LSTM RNN-based excitation force prediction for the real-time control of wave energy converters

Ming Zhang [a], Zhi-Ming Yuan [a,*], Sai-Shuai Dai [a], Ming-Lu Chen [b], Atilla Incecik [a]

[a] Department of Naval Architecture, Ocean and Marine Engineering, University of Strathclyde, 100 Montrose Street, Glasgow, G4 0LZ, UK
[b] School of Naval Architecture & Ocean Engineering, Jiangsu University of Science and Technology, 2, Mengxi Road, Zhenjiang, 212003, Jiangsu, China

ARTICLE INFO

ABSTRACT

Wave energy is a type of abundant and dense renewable energy. Wave force prediction is a critical technology that influences power absorption efficiency in the real-time control of wave energy converter (WEC). Could wave elevation be used to predict wave excitation force directly by training artificial neural network? This method results in rapid and suitable prediction for real-time control. A long short-term memory recurrent neural network (LSTM RNN) algorithm is introduced to identify characteristics of wave excitation forces based on wave elevations. In this method, the wave elevations in front of the structure are measured to obtain sufficient time to actuate the control manipulation. A total of 180 regular wave and 12 irregular wave tests are conducted, and the LSTM RNN model is trained based on the experimental results. The performance of the LSTM algorithm is verified. According to the regular cases in the study, the LSTM prediction can identify high-order harmonic loads, and the anti-noise capability of the LSTM algorithm can filter random noises from the measure signals. In the irregular cases, the LSTM RNN algorithm performs effectively to predict the wave force excited on the structure using wave elevations measured by wave probes. The best combinations of the test setting parameters are determined to guide experimental tests and WEC prototypes.

1. Introduction

Ocean renewable energy receives increasing worldwide attention for its capability to satisfy the energy demand worldwide. Thus, fossil fuel saving and reduction of carbon emissions can be achieved simultaneously. In addition, it stimulates economic development in coastal areas. Among various ocean energy sources including wind, wave, current, tide and thermal, the potential associated with wave energy is approximately 28,000 TWh per year (Jin, 2019). It can supply 10% of European electricity requirements or generate the equivalent of up to 20% of UK electricity.

A wave energy converter (WEC) is a device used to produce electrical energy from wave-induced motion. To harvest the ocean wave energy, thousands of concepts of wave energy converters have been proposed. One of the key aspects for maximising the energy yield of many WECs is the control of the dynamic response of the device to wave conditions (Korde and Ringwood, 2016). The response control of the WEC captor or primary converter is to transfer energy from wave to oscillating body via the power-take off (PTO) system; it is responsible for further energy conversion, generally to electricity. The control of WEC from wave energy to electricity is known as the Wave-to-Wire

(W2 W) system. Although WEC technologies have been developed for decades, no WEC has reached commercial stage due to its high levelised cost of energy (LCOE). One way to move forward is improving the power absorption efficiency with real-time control. The velocity of WEC can be tuned with the excitation force of incoming wave to achieve the maximum energy absorption by controlling the force exerted from the PTO system.

Recent research focuses on types of real-time control of WECs, including reactive control (Salter, 1979), latching control (Li et al., 2018a), declutching control (Babarit et al., 2009) and Model Predictive Control (MPC) (Li and Belmont, 2014). For these power maximisation control strategies, the future information of excitation force is compulsory and essential. The two alternative approaches to obtain the wave excitation force are as follows: (1) the total wave force is measured using pressure transducers installed on the WEC wet surface; (2) the excitation force from the wave elevation measurement with wave probes is calculated. The former requires precise mathematical description of hydrodynamic distribution, and the latter is a challenging problem due to its nonlinearity and noncausality. For implementation of many energy maximising control strategies, two processes require

---

future knowledge of the incoming wave experienced by WEC (Garcia-Abril et al., 2017). Falnes (1995) described the noncausal characteristic of wave excitation force deduced by wave elevation; information on future wave elevation is necessary. Fusco and Ringwood (2012) and Son and Yeung (2017) assumed that the in-coming wave elevation is known fully or in the near future. The excitation force is indirectly measurable for oscillating WECs. Thus, the excitation force estimation with reasonable accuracy is critical for real-time power maximisation control of WEC systems. Some researchers realised wave force prediction by using alternative methods. An LSTM-NARX hybrid network was proposed to predict wave excitation force based on noncausality (Zhang et al., 2020), but the accumulation of errors worsens the accuracy of the simulation results. A linear superposition (Li et al., 2012) and a Kalman Filter (Ling, 2015) were used in control implementation of WEC. Hillis et al. (2020) proposed two methods of force estimation based on Kalman filters with an experimental 1 : 25th scale multiple degree-of-freedom WEC. Nguyen and Tona (2017) evaluated two methods of wave force estimation by using actual measurements from a laboratory scale WEC. One disadvantage of these methods is that they predicted the future excitation force based on the current force, in which the performance of prediction decreases with the extension of prediction horizon. A robust and succinct force estimation, which is insensitive to the prediction horizon should be applied to real-time control practice.

As an explosive development of Artificial Intelligence and Machine Learning application in the last decade, more research fields (image processing, speech recognition, medicine, power grid and automatic control) introduce some 'pop-stars' of machine learning to solve traditional problems in an unconventional approach. As a tool for time series prediction and modelling, artificial neural networks (ANNs) have been successfully used in various application domains, including financial time series prediction (Zhang, 2014), significant wave forecasting (Deo and Sridhar Naidu, 1998) and traffic prediction (Duan et al., 2016). Some researchers attempt to use ANN to optimise power absorption with control strategy. In Valério et al. (2008), ANN models for the Archimedes Wave Swing (AWS) prototype are developed. ANNs are then used together with proven control strategies (phase and amplitude control, internal model control and switching control) to maximise energy production. Li et al. (2018a) applied ANN to predict wave force to improve power efficiency of a heaving point absorber wave energy converter (HPAWEC) in which only offline simulation was discussed, but the performance of ANN prediction was not validated in the experimental test.

With the increase in complexity of application problems, the vanilla ANN becomes incompetent. Thus, LSTM RNN is introduced to solve the wave force prediction problem in the real-time control of WECs. As a branch of RNN architecture used in the field of deep learning (Hochreiter and Schmidhuber, 1997), LSTM RNN is first proposed in 1997; it outperforms the conventional approach. Gradient explosive and gradient vanishing problems are solved successfully (Greff et al., 2017). The LSTM model can learn to forget useless information and maintain long-term memory from the training dataset. LSTM RNN has been applied to tasks, such as unsegmented, connected handwriting recognition and speech recognition, because of its excellent performance when processing time-series information. LSTM algorithm has been applied to predict the power generation and WEC modelling (Neshat et al., 2019; Ni, 2021; Mousavi et al., 2021), but it is rarely used in wave prediction in real-time control of WEC (Rahoor, 2020). Applying an LSTM algorithm in the energy absorption maximisation of WEC is a promising solution.

Toward realising the real-time control of WEC in the experimental test, the present study focuses on the time series prediction of wave excitation force. The proposed wave force prediction method is evaluated using actual measurements from a laboratory scale HPAWEC in regular and irregular wave conditions. The wave elevations of incident waves are inputs of the LSTM training process. Based on the measured-experimental comparison in the time and frequency domains, the performance and advantages of the proposed approaches are discussed

in this study. The optimal distribution of wave probes is determined based on the deviation of predicted excitation force, which guides the future experimental setting of the proposed method. The highlights of the present research include the following:

(a) Introducing LSTM RNN machine learning algorithm to wave excitation force based on the data of experimental tests;
(b) Identifying the high-order harmonic loads of wave force and decreasing the influence of unexpected noises using LSTM RNN algorithm;
(c) Determining the optimal number of wave probes and spacing distance among input wave probes for experimental test of wave load measurement.

The paper is organised as follows. Section 2 introduces the experimental test model, including WEC model and experimental test setting. Section 3 introduces the LSTM prediction algorithm and data processing. The prediction results of wave force under regular and irregular waves are discussed in Section 4. Conclusion and future work are summarised in Section 5.

2. Prediction method of wave excitation force

2.1. Hydrodynamic model of HPAWEC

The linear potential flow theory is adopted to address the wave-structure interaction of HPAWEC (Li et al., 2018b). The vicious effect is neglected. The linear dynamic model is applicable without considering the extreme sea states because a full-scale WEC only works in a moderate sea state. Latching control strategy is used to maximise the power absorption. Based on the impulse response theory (Cummins, 1962), the time-domain motion equation of the floating body is expressed as Cummin's equation, as follows:

$$(M+m)\ddot{z}(t) + \int_0^t h(t-\tau)\dot{z}(\tau)d\tau + (C+c\beta(t))\dot{z}(t) + (K+\rho g\pi R^2)z(t) = F_{ex}(t), \tag{1}$$

where M is the mass of the floating body, and m is the added mass corresponding to infinite frequency. $\ddot{z}(t)$, $\dot{z}(\tau)$ and $z(t)$ are the acceleration, velocity and displacement, respectively. The convolution integral of the second term in the left-hand side is the memory effect of radiation force, where h is the retardation kernel function. C is the linear damping coefficient of the PTO. c is the additional damping of the latching control strategy. K and $(K+\rho g\pi R^2)$ are the restoring coefficients of the PTO and the floating body, respectively. F_{ex} is the wave excitation force. β is the control command calculated by the latching control strategy, such as MPC. The cost function of latching control is maximising the average absorption power of PTO, as follows:

$$\max P_{ave} = \frac{1}{T}\int_0^T C\dot{z}^2(\beta,t)dt. \tag{2}$$

The memory effect of wave is expressed in a state space representative by using system identification; thus, implementing the control strategy becomes convenient.

$$\begin{aligned}\vec{C}u &= \int_0^t h(t-\tau)\dot{z}(\tau)d\tau \\ \dot{u} &= \vec{A}u + \vec{B}\dot{z}\end{aligned}. \tag{3}$$

Therefore, the hydrodynamic equation is rewritten in a state space as follows:

$$\begin{aligned}\dot{x} &= \gamma \cdot x + \eta \\ x &= \begin{bmatrix} z & \dot{z} & u \end{bmatrix}^T \\ \gamma &= \begin{bmatrix} 0 & 1 & 0 \\ -\frac{K+\rho g\pi R^2}{M+m} & -\frac{C+c\beta}{M+m} & -\frac{\vec{C}}{M+m} \\ 0 & \vec{B} & \vec{A} \end{bmatrix} \\ \eta &= \begin{bmatrix} 0 \\ \frac{F_{ex}}{M+m} \\ 0 \end{bmatrix}\end{aligned} \tag{4}$$
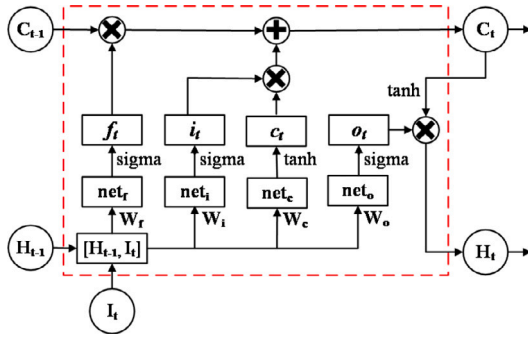
Fig. 1. Memory block architecture of LSTM RNN.

The only unknown variable in Eq. 4 is the wave excitation force F_{ex}. Once F_{ex} is predicted or estimated with a high accuracy, the motion response of the floating body is controlled by Eq. 4 to optimise the power capture.

2.2. LSTM RNN model

As shown in the introduction section, the excitation force is derived from the entire information of wave elevation. An LSTM RNN, whose inputs are wave elevations and outputs are forces, is required to represent the relationship due to the noncausal relationship between wave force and wave elevation (Falnes, 1995). The memory block architecture, which is the core of LSTM RNN, is shown in Fig. 1. I_t is the input of the *t*th time step. H_t is the hidden unit of the *t*th time step. C_t is the state cell of the *t*th time step. Constant Error Carousel (CEC), which can 'keep memory' of characteristics in the time series, is in the red dash rectangle. The input gate, output gate and forget gate are inside the CEC. Information is transformed through CEC between gates and state cells. The gates control information flow and transmit information between short-term memory and long-term memory, and state cell stores the long-term time-series memory. LSTM RNN is regarded as a deep learning architecture because of the existing of memory block. The expression of the memory block is as follows:

$$
\begin{aligned}
f_t &= \sigma(y_f) = \sigma(\omega_f \cdot x + b_f) \\
i_t &= \sigma(y_i) = \sigma(\omega_i \cdot x + b_i) \\
o_t &= \sigma(y_o) = \sigma(\omega_o \cdot x + b_o) \\
\tilde{c}_t &= \tanh(y_{\tilde{c}}) = \tanh(\omega_c \cdot x + b_c) \\
c_t &= f_t \times c_{t-1} + i_t \times \tilde{c}_t \\
h_t &= o_t \times \tanh(c_t)
\end{aligned}
\tag{5}
$$

where the subscripts f, i and o represent the forget gate, the input gate and the output gate, respectively. σ is the sigmoid function as the most used activation function in different types of neural network, and $\tanh$ is the mathematical operator of hyperbolic tangent function. The operator $\times$ is a multiple operation of matrices (Zhao et al., 2019).

In the architecture of the proposed LSTM RNN, the wave heights recorded by wave probes are system inputs, and the wave excitation of load cell represents system output. It is a multi-input/single-output (MISO) system, but the proposed algorithm is also suitable to analyse multi-input/multi-output (MIMO) system for solving multibody motions or coupled multidegree-of-freedom motion problems. Mathematically, to realise the W2EF prediction, the information of wave excitation force is ahead that of wave elevation in the training and test dataset. In this extent, the well-trained network reflects the relationship of current wave and future wave force although the relationship is noncausal.

Table 1
The parameters of the cylindrical buoy.

Parameter	Symbol	Unit	Value
Buoy radius	R	m	0.10
Buoy draught	D	m	0.28
Buoy mass	M	kg	9.00
Hydrostatic stiffness	K	N/m	315.30
Added mass at infinite frequency	m	kg	2.03

2.3. Data processing

Data pre-process is necessary prior to training the network. Normalisation is beneficial to the convergence of neural network training. The weight gradients vary in the same magnitude because all the inputs are in the same magnitude, thereby eliminating the error caused by the different parameter ranges. The standardised normalisation is used to pre-process the measured data.

$$
\begin{aligned}
x_w &= \frac{X_w - \mu_w}{\sigma_w} \\
x_f &= \frac{X_f - \mu_f}{\sigma_f},
\end{aligned}
\tag{6}
$$

where x represents the standardised value which is distributed as $N \sim (0,1)$. X represents the measured value before standardisation, which is distributed as $N \sim (\mu, \sigma^2)$. μ is the expected value, and σ is the standard deviation. The subscripts, w and f, represent wave elevation and excitation force, respectively. The calculation of predicted forces requires a denormalised process to restore the magnitude of measured values. Root mean square error (RMSE) is usually used to express the deviation of prediction from the measured value.

$$
\text{RMSE} = \sqrt{\frac{\sum_1^N (y - \hat{y})^2}{N}}.
\tag{7}
$$

However, the amplitude of the measured value y influences the value of RMSE. To eliminate the impact of the amplitude of y, a normalised RMSE (NRMSE) is calculated to evaluate the accuracy of the prediction results.

$$
\text{NRMSE} = \text{RMSE}/\left(\frac{y_{\max} - y_{\min}}{2}\right),
\tag{8}
$$

where y_{max} is the maximum value, and y_{min} is the minimum value. The denominator in Eq. (8) represents a characteristic amplitude of the measured value. Under the circumstances, the prediction results of different wave heights can be compared to evaluate the performance of LSTM prediction algorithm.

3. Experimental test model

3.1. Wave energy converter model

To verify the proposed excitation force modelling approaches, a 1/25 model-scale cylindrical heaving point absorber wave energy converter (HPAWEC) was designed, constructed and tested in the Kelvin Hydrodynamics Laboratory (KHL) at the University of Strathclyde, as illustrated in Fig. 2. A fixed type wave structure interaction is investigated; it neglects the influence of motion response to the wave elevation. The scale of the wave tank is 6 m × 3.5 m × 1 m. The buoy dimensions are hydrodynamic coefficients estimated by software SESAM WADAM, as shown in Table 1. The actual nature frequency of the buoy structure is slightly lower than the simulated value because the viscous effect is not considered.
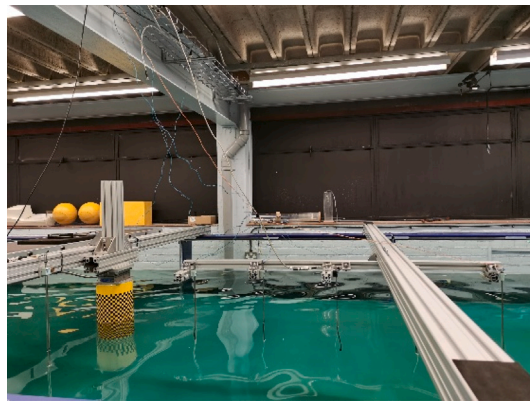
3.2. Experimental test settings

A wide variety of wave tank tests were conducted under regular wave conditions for verification of the proposed LSTM prediction method, as shown in Table 2. The variation of the number of WPs
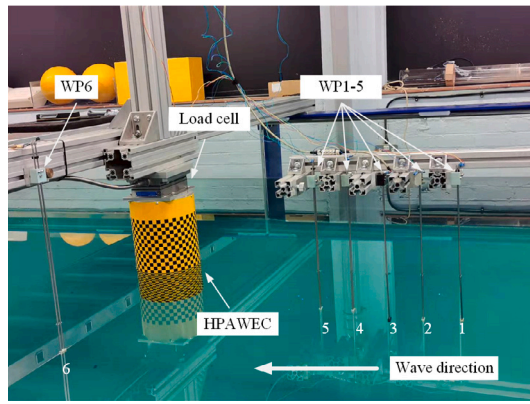
(a) $d = 0.1$m

(b) $d = 0.4$m

Fig. 2. Measurement calibration and validation of load cell.

Table 2
Parameter setting of the regular wave tests.

| Parameter	Symbol	Unit	Value
Number of WPs	N		1, 2, 3, 4, 5
Spacing of WPs	d	m	0.10, 0.20, 0.30, 0.40
Wave height	H	m	0.01, 0.02, 0.04, 0.06, 0.08
Wave frequency	f_w	Hz	0.30 : 0.10 : 1.10

is used to determine the optimal number, N. The effective range of the input WPs is less than 2 m given the finite length of the wave tank in KHL and the existence of HPAWEC model. The maximum spacing is determined as 0.4 m with five WPs. The interference between neighbouring WPs affects the measurement of wave elevations if the spacing is less than 0.05 m. Therefore, the spacing is 0.10 : 0.10 : 0.40 m. The measurement of the spacing is $d \pm 0.001$ m. The wave height of the regular wave varies from 0.01 m to 0.08 m. The wave frequency varied in a wide range (0.30 – 1.10 Hz), and the frequency increment is densified near the natural frequency of the HPAWEC structure. If $H > 0.80$ m or $f_w > 1.10$ Hz, then the wave is deformed as the nonlinear components. The distance between the centre of the structure model and the last wave probe (WP5) is fixed at 0.54 m. Test cases were conducted under irregular wave conditions, as shown in Table 3. The number of WPs and the spacing between neighbouring WPs vary, the same as the regular cases. The HPAWEC was scaled down according to the Froude number. Therefore, the time ratio was $1/5$. The characteristics of ocean waves of sea states 3 and 4 defined by the Beaufort scale can be represented by a PM spectrum with significant wave height H_s and peak frequency f_p. The wave characteristics of the scaled down PM spectrum are listed in three cases ($f_p = 0.65, 0.7, 0.8$ Hz) in Table 3. For the sake of simplicity, the wave elevation generated in wave tank is single directional. The wave elevation satisfies

Table 3
Parameter setting of the irregular wave tests.

	Significant height H_s (m)	Peak frequency f_p (Hz)
Case 1	0.93	0.65
Case 2	−0.8	0.7
Case 3	0.063	0.8

(a) Load cell and weights
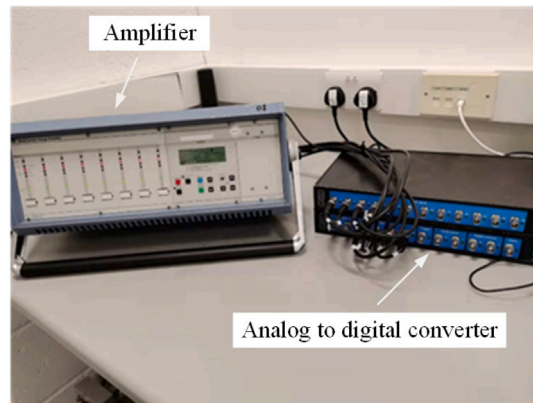
(b) Amplifier and analog to digital converter

Fig. 3. Measurement calibration of load cell.

the assumption of the linear wave theory because the ratio of wave amplitude to the wave length is $A/\lambda \ll 1$.

3.3. Calibration of load cell and wave probes

The measurement calibration of load cell is shown in Fig. 3. The analogue signal of the load cell is amplified by the amplifier and converted into digital signal, which is shown in scopes. Normally, the load in heave direction is used in the study of a HPAWEC, which is related to power efficiency. However, in the experimental test of
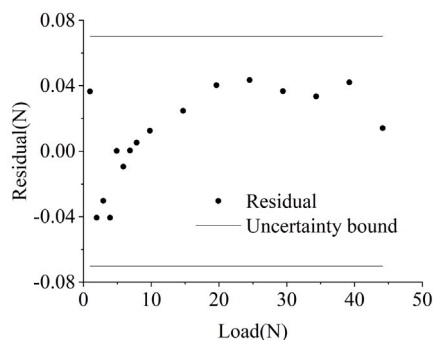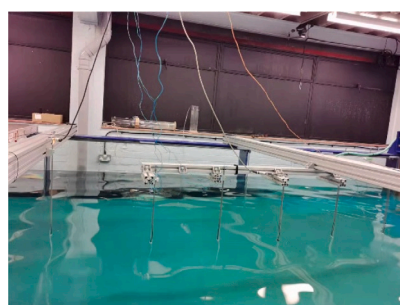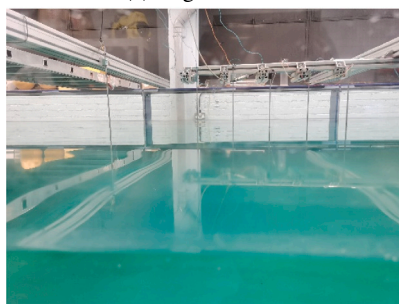
Fig. 4. Measured uncertainty band and validation of the load cell.

(a) Regular view

(b) Side view

Fig. 5. Measurement calibration of wave probes.

Table 4
Hyperparameters of the LSTM algorithm for the regular wave cases.

Parameter	Symbol	Unit	Value
Sampling frequency of dataset	f_s	Hz	100
Forward time	T_f	s	5
Total time	T_{total}	s	100
Ratio of training data	R_{train}		0.8
Initial learning rate	$LR_{initial}$		0.01
Drop period of learning rate	N_{drop}		50
Number of LSTM hidden units	N_h		5
Iteration loops	N_{loop}		150

4. Results and discussions

4.1. Performance of the uni-directional regular wave prediction

The normalised wave elevations and excitation forces are shown in Fig. 8. The signals have been filtered by a low-pass filter of 1.8 Hz cut-off frequency. An interpolation is carried out to generate training data (f_s = 100 Hz) from test data collection (f_s = 1000 Hz). Prior to the training process, the dataset is normalised with mean 0 and standard deviation 1 ($\mu = 0, \sigma = 1$); thus, the training processes converge fast. The black curves are the inputs of prediction algorithm, and the red curve is the output. The curves of wave elevations collected from the tests are not the perfect sinusoidal signal. Several reasons cause these imperfect elevations. Firstly, the wave elevations are approximately generated by the wave pedals in the wave tank of finite scales. The waves are influenced by motion deviations of wave pedals, and the reflection waves deform the incident waves as well. Once the waves propagate, the measured elevation does not become the sinusoidal wave. Secondly, measurement uncertainties and measurement deviation are shown 8. Similar non-harmonic phenomena is observed in wave excitation forces, as shown in the red curve. The nonlinearity is more evident in the force curve. This is because the measured force contains high-order components. In addition, the structure responses contain components of high-order loads. The measured signals without curve fitting are used to verify the robustness of the prediction algorithm because uncertainties and disturbances exist in actual applications. The measured data show time lag of wave propagation from WP1 to WP5 given that the WPs are placed in different positions in the wave propagation direction. The same hyperparameters of LSTM machine learning algorithm can be predefined for all the cases because the signals have been normalised to eliminate 'scale effect' of amplitude. The hyperparameters are listed in Table 4. The total time of 100 s contained sufficient wave periods for all frequencies. Even for cases of f_w = 1.1 Hz, the training dataset still has more than 70 wave periods. The signals of regular wave only contain components of one foundational frequency and corresponding high-order frequency; thus, the architecture of the LSTM network can be shallow. The network becomes deeper in irregular wave conditions because of the various frequency components. Some representative results of the wave force prediction are shown in Fig. 9 to illustrate the performance of the LSTM algorithm. NRMSE represents deviations between the predicted forces by LSTM algorithm and the measured forces of tests. Thus, results of different wave heights can be compared fairly with the same magnitude. The low NRSME indicates good performance of the prediction algorithm. The LSTM algorithm can predict the excitation forces, which agree with the measured forces when the signals have high quality. The LSTM algorithm can recognise the one-order load and the high-order harmonic loads shown in the power density of frequency domain. Except these specific frequencies, the responses are suppressed as low magnitudes. The unexpected fluctuations of time history curves caused by noises are filtered by LSTM algorithm. It is similar to the LSTM algorithm that trains the network model; *remember* the dominant and regular things, and *forget* all the random and irregular things.
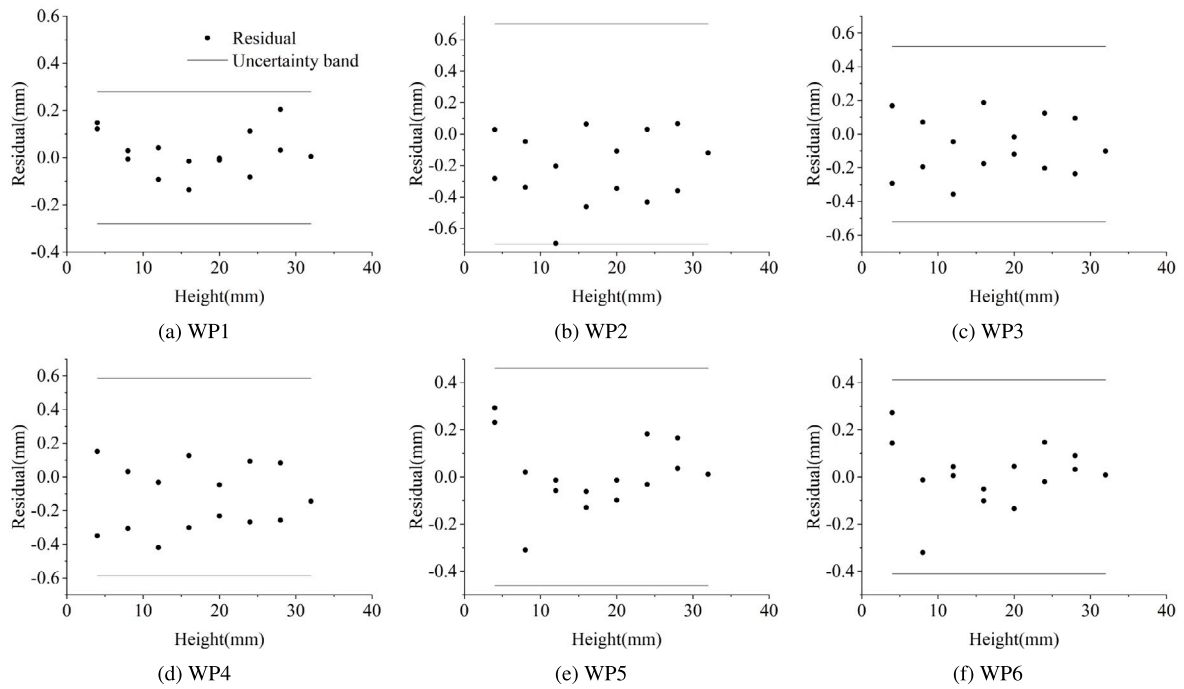
the presented study, the heave excitation force of the model scale (1 : 25) is extremely small and the magnitude is at the same level as the noise of the measured signal. Fortunately, the load in the surge direction is sufficiently large because of the large section area. To illustrate the results clearer and straightforward, the excitation force is recorded and compared. The weights loaded vary from 100 g to 5000 g to calibrate the accuracy of the load cell. The uncertainty band of the measurement calibration and the load cell validation are shown in Fig. 4. The peak values of the excitation force in the test are larger than 20 N, and the uncertainties of the load cell are smaller than 0.07 N. The calibration setting of wave probes is shown in Fig. 5. The wave probes are distributed and aligned in the middle of the width, which reduces the influence of the reflection wave from the side walls. The measurement calibration and validation of wave probes are shown in Fig. 6. The largest uncertainty of all the wave probes is 0.7 mm. The measurement uncertainties of the load cell are acceptable in the series of model tests. The uncertainties cause unreliability of the prediction results. The data inside the uncertainty bands are reliable, and the data outside uncertainty bands are induced by prediction deviation (see Fig. 7).

Fig. 6. Measured uncertainty band and validation of wave probes.
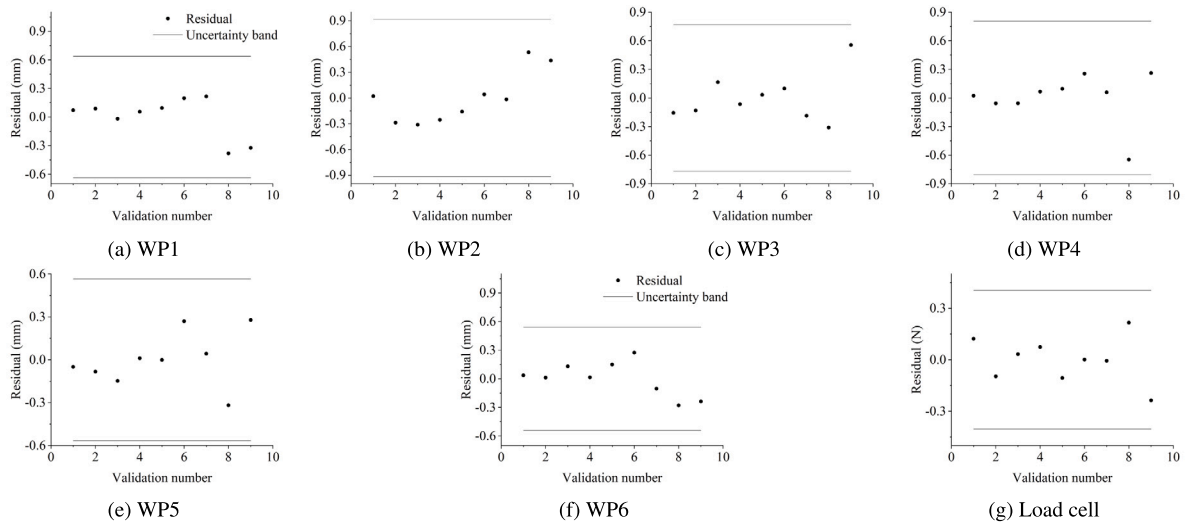

Fig. 7. Measurement deviation of wave probes and load cell.

As shown in Fig. 9(a), when the wave frequency and the wave height are high, the signal of the measured force has high quality in the signal-to-noise ratio (SNR). The predicted force is almost regressive to the measured force in the time domain. Moreover, the trough value of the predicted force is more stable than that of the measured force. The subfigure in the frequency domain in Fig. 9(a) shows that the LSTM algorithm only passes the components of the leading order (0.85 Hz) and the corresponding high-order frequencies (1.70 and 2.55 Hz). The force curve in the time domain is similar to a sinusoid curve because the energy density of the leading order frequency is much larger than that of corresponding high-order frequencies. If the incident wave frequency becomes low, then the ratio of the high-order harmonic loads increases, as shown in Fig. 9(b). The time domain signal is deviated significantly from the sinusoidal curve. The crests are flattened and the troughs are sharpened due to the high-order force components. If the wave height and the incident wave frequency are low, then the SNR is extremely low to measure the expected signal, as shown in Fig. 9(c). The energy

density of noise signal under 1.0 Hz is the same as the magnitude of the incident wave frequency (0.3 Hz). Thus, the noises have distorted the measured signal far away from the sinusoidal curve. After the processing of LSTM prediction, the envelop of the force curve is a sinusoidal curve with the incident wave frequency, and the crests and troughs are influenced by high-order components more evidently than those in Fig. 9(b).

In Fig. 9(c), the noises in the frequency domain of the measured signal have the same magnitude of power density as the signal of incident wave frequency and its harmonic loads. The force per unit wave amplitude of the measured force in time domain is influenced by random noise seriously. After the processing of the LSTM, it extracts the leading-order load of f_w and its corresponding harmonic loads. The fluctuations caused by the unexpected noises are filtered by the LSTM neural network. This finding indicates that the LSTM algorithm would be an additional process to improve the SNR of the time–history signal. When analysing the interaction of a small structure in an extreme
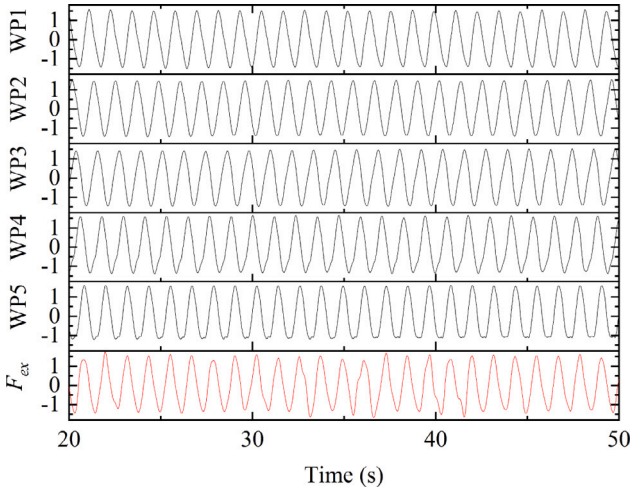
Fig. 8. Normalised wave elevations and excitation forces of regular wave ($N = 5$, f_w = 0.85 Hz, H = 0.08 m, d = 0.4 m).

(a) $H = 0.02$ m

(b) $H = 0.04$ m

(c) $H = 0.06$ m

(d) $H = 0.08$ m

Fig. 10. NRMSEs of the prediction results of regular wave tests against N and f_w.

(a) $f_w = 0.85$ Hz, $H = 0.08$ m, NRMSE = 0.036

(b) $f_w = 0.3$ Hz, $H = 0.08$ m, NRMSE = 0.134

(c) $f_w = 0.3$ Hz, $H = 0.01$ m, NRMSE = 0.223

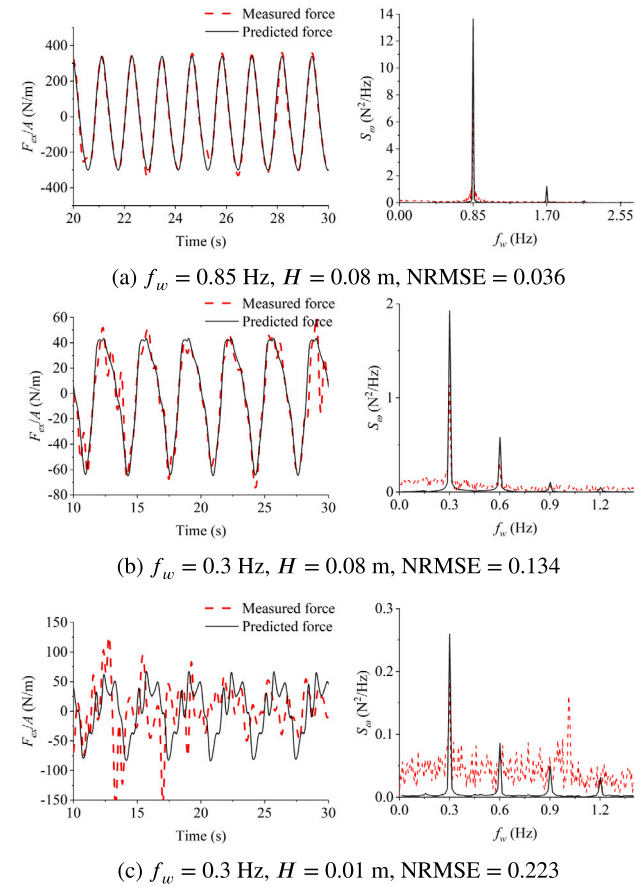Fig. 9. Predicted force of LSTM algorithm in regular wave ($N = 5$, $d = 0.4$ m, left: force in time domain, middle: force spectral density, right: force spectral density near incident wave frequency).

environment, the wave height is high and the structure characteristic dimension is the same as the magnitude of the wave height. When balancing the limit of wave frequency and wave height in a model-scaled experimental test, the dimensions of the model-scaled structure and incident wave frequency have small values. In this condition, the result of wave excitation force likely has low-quality, as shown in
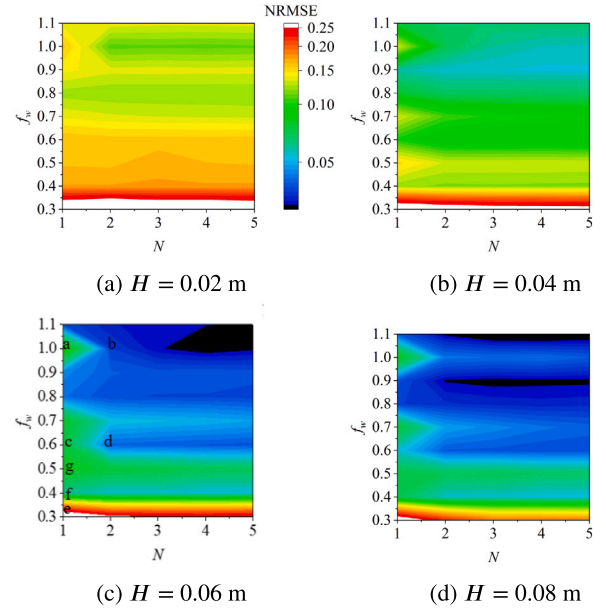
Fig. 9(c). The LSTM can provide a reliable result without spikes caused by these random noises.

One of the aims of this research is to identify the best number of wave probe and spacing distance of wave probe for the wave excitation force prediction based on LSTM algorithm. Thus, the prediction results of different N and d combinations are shown as contours to determine the optimal range. The contours of the NRMSEs of regular wave results against N and f_w are shown in Fig. 10. For regular wave, if the NRMSE > 0.25, then the errors are extremely large to represent the measured data, which have white colour. If NRMSE > 0.03, then the results are shown as black colour. The NRMSE of each combination of N and f_w is the average value of four spacing distances. The best performance of LSTM algorithm is 0.0476 when $N = 4$, $f_w = 1.0$ Hz and $H = 0.06$ m. The NRMSE decreases with the significant increases in H, which is not caused by the LSTM algorithm but mainly by the SNR improvement. In terms of the number of wave probes, increasing N from 1 to 2 decreases the NRMSE significantly under specific wave frequencies ($f_w = 0.6$ and 1.0 Hz) in most wave height. This drop in NRMSE is not evident under other wave frequencies. The decrease is caused by different factors. When $f_w = 1.0$ Hz and $d = 0.3$ m, the predicted force of $N = 1$ has a phase shift compared with the measured force, as shown in Fig. 11(a). Although only one-step shift exists, the NRMSE increases because the deviation is accumulated in each time step. When N increases to 2, the phase shift is eliminated, as shown in Fig. 11(b). When $f_w = 0.6$ Hz and $d = 0.4$ m, no phase shift occurs, but fluctuation exists at the troughs for case of $N = 1$, as shown in Fig. 11(c). The fluctuation is eliminated by increasing N to 2 in Fig. 11(d). Thus, at these ranges, the deviations of predicted forces decrease when N rises from 1 to 2, and then it maintains a stable value when N increases to a higher value. Except these unusual ranges, the performance of LSTM algorithm is improved slightly with the increase in N. The second input of wave elevation can compensate the inaccuracy, which exists in sole input condition. More than two inputs of wave elevations contribute slightly to the improvement of the results in regular wave conditions. The finding indicates that the performance is insensitive to N when $N > 1$. The performance is improved when the incident wave frequency varies from 0.3 Hz to 0.5 Hz ($d = 0.4$ m) mainly caused by SNR improvement, as shown in Figs. 11(e)–11(g). In each contour of Fig. 10, the decrease in NRMSE agrees with the force curves of time history.
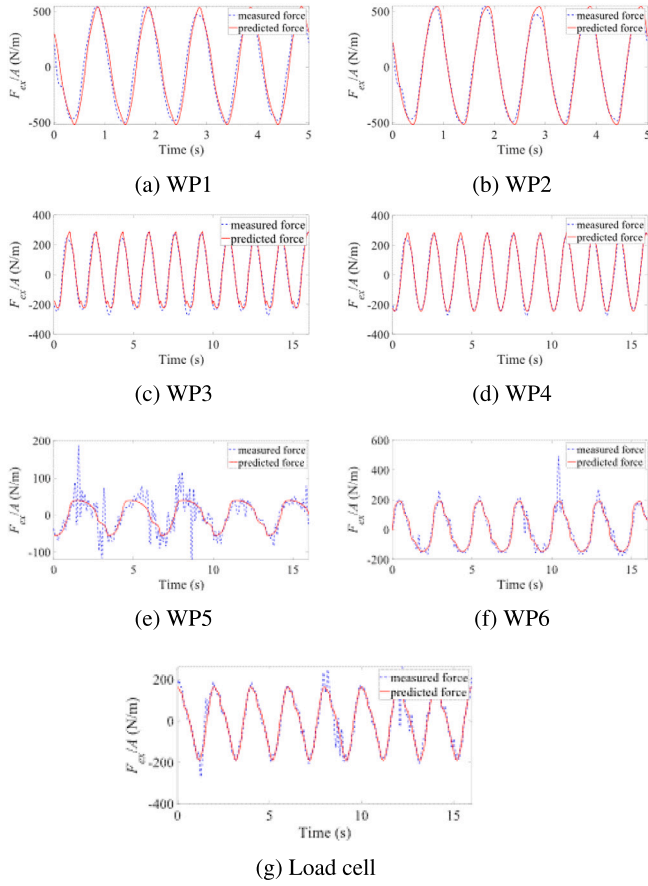
(a) WP1

(b) WP2

(c) WP3

(d) WP4

(e) WP5

(f) WP6

(g) Load cell

Fig. 11. Predicted excitation force in time domain (H = 0.06 m).

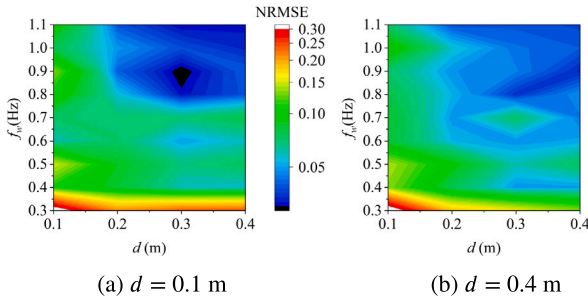

(a) d = 0.1 m

(b) d = 0.4 m

Fig. 12. NRMSEs of the prediction results of regular wave tests against d and f_w (N = 4).

The contours of the NRMSEs of regular wave results against d and f_w are shown in Fig. 12. Only H = 0.06 and 0.08 m are shown here to determine the best spacing. Different from the average value of four cases of d, the lowest value of NRMSE, 0.02805, is simulated when H = 0.06 m, d = 0.3 m and f_w = 0.9 Hz, as shown in Fig. 12(a). When d = 0.3 m, sub-optimal solutions are obtained when f_w = 0.4 and 0.6 Hz. Whether the spacing increases or decreases, the performance is worse than that of d = 0.3 m. Combining the results shown in Figs. 10 and 12, the best setting of wave probes is N = 4 and d = 0.3 m. The best setting for regular wave is a guide for setting the irregular wave discussed in the following section (see Fig. 13).
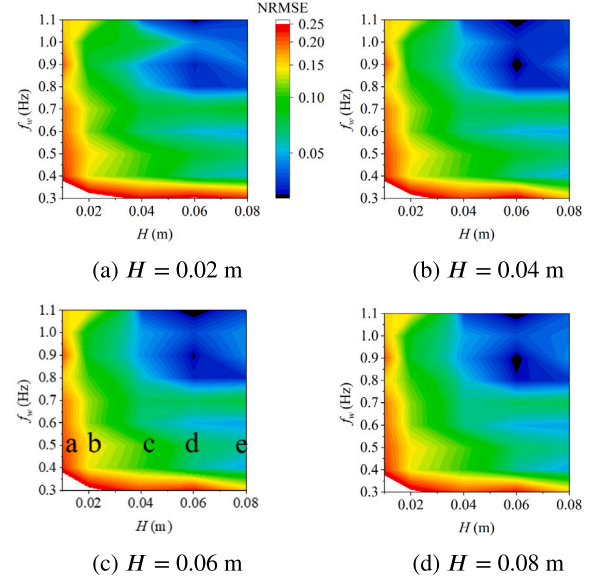

(a) H = 0.02 m

(b) H = 0.04 m

(c) H = 0.06 m

(d) H = 0.08 m

Fig. 13. NRMSEs of the prediction results of regular wave tests against H and f_w (d = 0.3 m).

4.2. Performance of the uni-directional irregular wave prediction

Each irregular wave elevation is propagated for 2400 s (2/3 h) in the model test because the model scale is 1 : 25; it is equivalent to a three-hour sea state in full scale. The normalised wave elevations and force excited on the structure are shown in Fig. 15. Group velocities of different frequency components are different due to the dispersion relation. Thus, the differences between WPs are not only the phases, but also the amplitudes. For the irregular wave cases, the hyperparameters of the LSTM algorithm shown in Table 5 is mostly larger than those in the regular wave cases because of the complicated frequency components. Time duration is set at 2000 s, 90% of the dataset is used for training, and 10% is used to validate the performance of the trained network. N_{drop}, N_h and N_{loop} increase to obtain a more accurate predicted force for irregular waves. f_s and T_f varied to investigate the sensitivities of prediction algorithm to the sampling frequency and the forward time. In the legend of Fig. 16(a), f_p is the peak frequency of PM spectrum, and mean indicates the average value of different spacing of wave probes. The lowest NRMSE is achieved when f_s = 10 Hz. The LSTM algorithm is insensitive to f_p because the best performance exists at the same f_s when the peak frequency of incident wave varies. If f_s is extremely high, then excessive local details of the training dataset cause overfitting of the LSTM network, as shown in Fig. 16(b). On the contrary, if f_s is extremely low, high-frequency fluctuations are filtered in the training dataset. The LSTM network cannot predict the high-frequency fluctuations if the fluctuations do not exist in the training dataset because the prediction is based on the trained network learning from the training dataset. The results of f_s = 5 Hz cannot capture the peak of the measured force, as shown in Fig. 16(c). The results of LSTM prediction in the irregular wave conditions are shown in Fig. 17. The legend in Fig. 17(a) has the same expression of Fig. 16(a). The best performance is achieved when T_f = 2 s regardless of the peak frequency of the sea state. When the forward time T_f increases from 0 s to 2 s, the NRMSE decreases gradually. When T_f varies from 2 s to 3 s, the NRMSE increases slightly. The deviation is still acceptable when T_f = 3 s, as shown in Fig. 17(b). The NRMSE increases dramatically if T_f > 3 s, indicating that the force curve in the time domain deviates from the measured force significantly, as shown in Fig. 17(b). The spectral densities of T_f = 0 s and T_f = 3 s agree with the spectral densities of
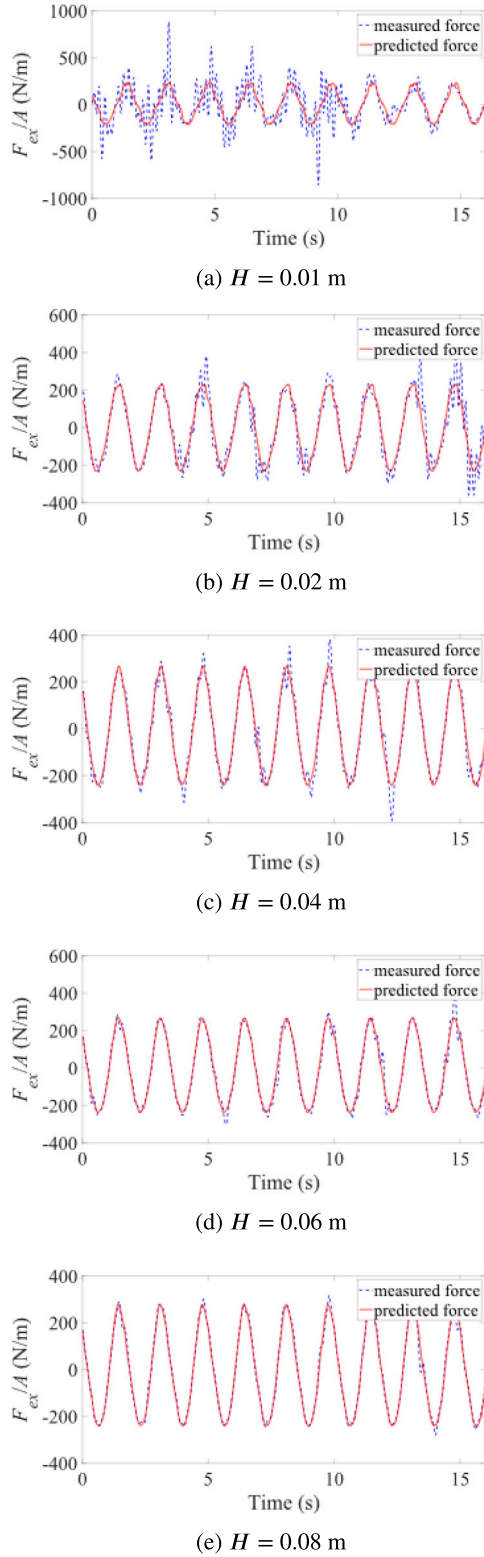
(a) $H = 0.01$ m

(b) $H = 0.02$ m

(c) $H = 0.04$ m

(d) $H = 0.06$ m

(e) $H = 0.08$ m

Fig. 14. Predicted excitation force in time domain against H ($f_w = 0.5$ Hz, $N = 4$, $d = 0.3$ m).

Fig. 15. Normalised wave elevations and excitation forces of irregular wave ($N = 5$, $f_p = 0.65$ Hz, $H = 0.105$ m, $d = 0.4$ m).

Table 5
Hyperparameters of the LSTM algorithm for the irregular wave cases.

Parameter	Symbol	Unit	Value
Sampling frequency of dataset	f_s	Hz	5–50
Forward time	T_f	s	1–3.6
Total time	T_{total}	s	2400
Ratio of training data	R_{train}		0.9
Initial learning rate	$LR_{initial}$		0.01
Drop period of learning rate	N_{drop}		100
Number of LSTM hidden units	N_h		100
Iteration loops	N_{loop}		400

and processing in the paper is about real-value time-series signals. Thus, the operation of complex conjugate is not considered. Cross-correlation coefficient of discrete signals can be expressed by

$$\rho_{XY}(X_{t_1}, Y_{t_2}) = \frac{E[X_{t_1} Y_{t_2}] - E[X_{t_1}]E[Y_{t_2}]}{\sqrt{E[X_{t_1}^2] - (E[X_{t_1}])^2}\sqrt{E[Y_{t_2}^2] - (E[Y_{t_2}])^2}}, \quad (9)$$

where ρ_{XY} is cross-correlation coefficient of two signals (X and Y). In the present study, X is the wave elevation, Y is the wave force, E is the expectation of signals. $\rho_{XY} = 1$ indicates a positive correlation, while $\rho_{XY} = -1$ indicates a negative correlation. Both positive and negative correlations are beneficial to training the machine learning model. $\rho_{XY,max}$ is a statistical value representing the maximum absolute value of the cross-correlation coefficients, and it can be expressed as follow,

$$\rho_{XY,max} = \max(|\rho_{XY}(WP, force)|) \quad (10)$$

Fig. 17(d) shows the result of $\rho_{XY,max}$ against T_f. $\rho_{XY,max}$ is subject to a sharp drop at $T_f > 3.2$ s in the case of $f_p = 0.65$ Hz.

The forward time limits the lowest efficiency of the control system. The control command should be calculated in 3.0 s for each step. On the contrary, improving computational efficiency of the control system shortens the forward prediction horizon of the LSTM algorithm, which is beneficial to the accuracy of the wave prediction.

The performance of LSTM algorithm of the irregular wave cases are shown in Fig. 18. The performance is sensitive to N and d. The best performance is NRMSE = 0.061 when $N = 5$ and $d = 0.3$ m. The lowest NRMSE of the irregular wave case is more than twice that of the regular wave case because the finite number of wave probe N cannot reconstruct the original signal with infinite frequency components. The LSTM only captures the most dominant ones with limited inputs to memory the most important things in the learning process.

The performance will drop dramatically if d increases from 0.3 m to 0.4 m. This finding indicates that the large spacing is not beneficial to

measured force. However, the spectral densities of $T_f = 3.5$ s deviates from that of the measured force (see Fig. 14).

The prediction performance of LSTM algorithm significantly decreases when T_f increases from 3.0 s to 3.5 s. This can be explained by the signal processing theory. The present wave and force measurement
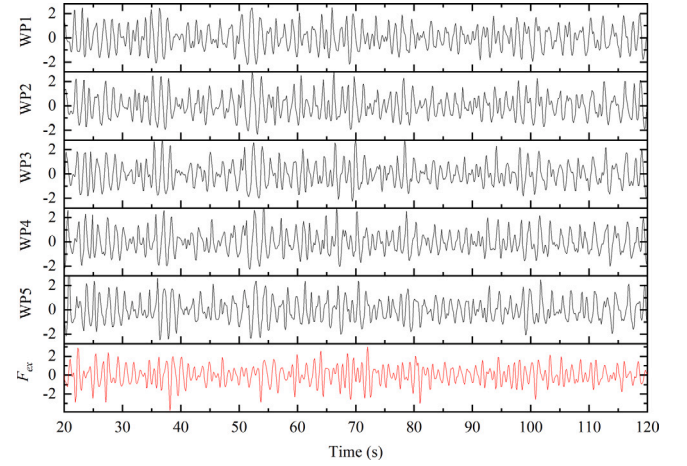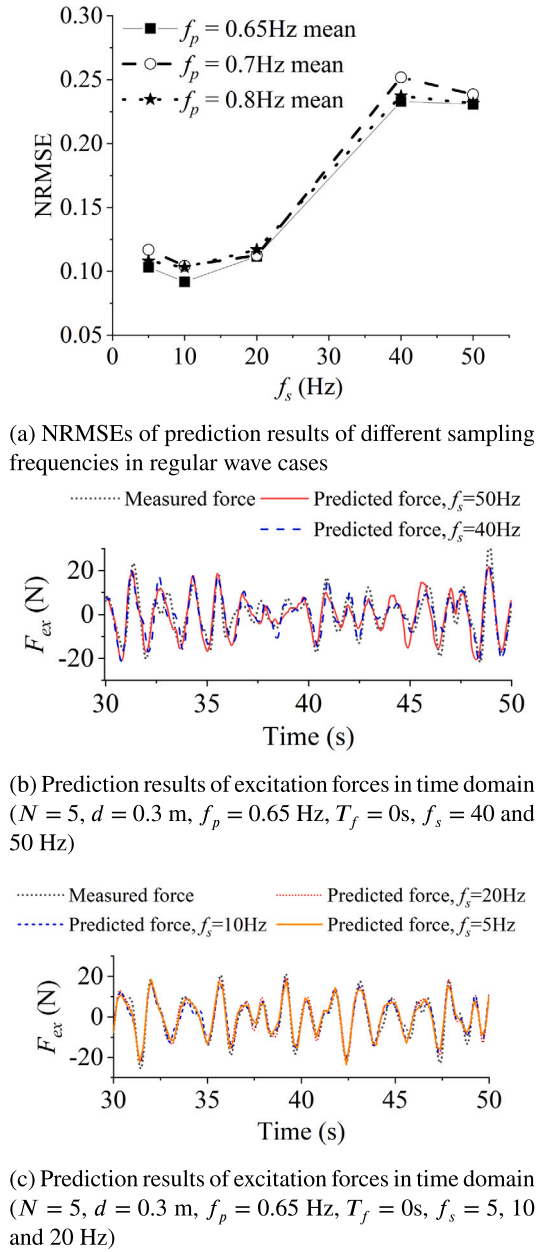
(a) NRMSEs of prediction results of different sampling frequencies in regular wave cases

(b) Prediction results of excitation forces in time domain ($N = 5$, $d = 0.3$ m, $f_p = 0.65$ Hz, $T_f = 0$s, $f_s = 40$ and 50 Hz)

(c) Prediction results of excitation forces in time domain ($N = 5$, $d = 0.3$ m, $f_p = 0.65$ Hz, $T_f = 0$s, $f_s = 5$, 10 and 20 Hz)

Fig. 16. Sensitivity of LSTM algorithm to the sampling frequency in irregular wave cases.

(a) NRMSEs of prediction results of different forward time in regular wave cases

(b) Prediction results of excitation forces in time domain ($N = 5$, $d = 0.3$ m, $f_p = 0.65$ Hz, $f_s = 10$ Hz)

(c) Spectral densities of excitation forces in frequency domain ($N = 5$, $d = 0.3$ m, $f_p = 0.65$ Hz, $f_s = 10$ Hz)

(d) The maximum absolute value of the cross-correlation coefficient ($D_{WP} = 0.3$ m, $f_p = 0.65$ Hz, $f_s = 20$ Hz).

Fig. 17. Sensitivity of LSTM algorithm to the forward time in irregular wave cases.

the performance of LSTM prediction. The force curve shown in Fig. 19 is the result at the black dash line in Fig. 18(c). Some local fluctuations cannot be captured when $N = 1$ (NRMSE = 0.097) or 2 (NRMSE = 0.079). When $N = 3$, the curve of the predicted force agrees with that of the measured force (NRMSE = 0.066). The time domain has no significant improvement of force curve from $N = 3$ (NRMSE = 0.066) to 5 (NRMSE = 0.061). $N = 3$ is sufficient to gain a good performance based on the simulation results of irregular waves in this study. $d = 0.3$ m is the best spacing, which agrees with the results of the regular wave cases.

4.3. Simulation of the multi-directional wave prediction

This subsection will discuss the capability of the adopted LSTM-based wave prediction for the multi-directional wave conditions. The feasibility of conducting multi-directional wave experimental tests and
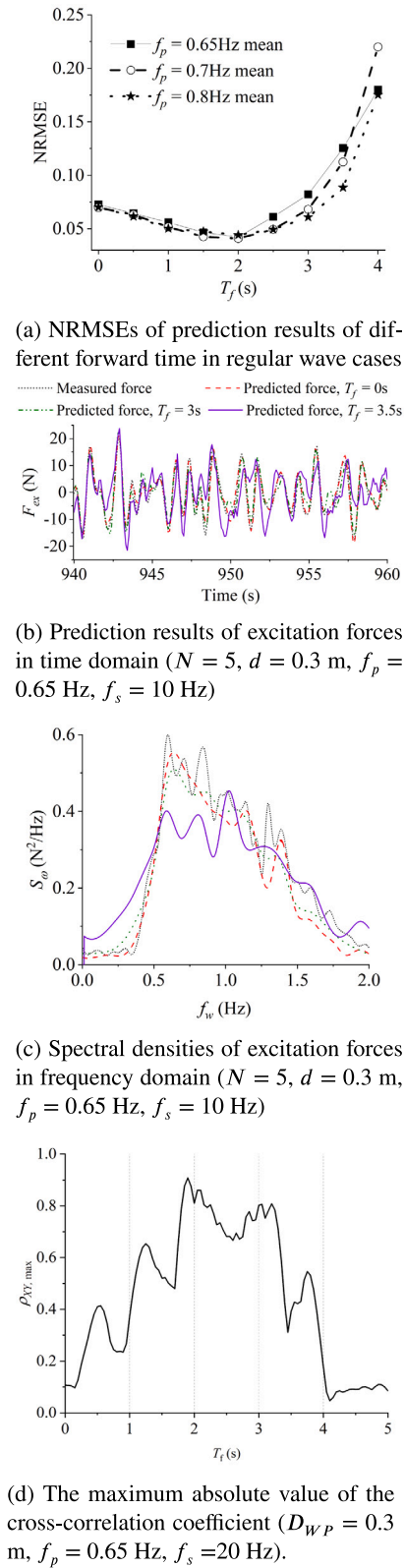
analysis at the Kelvin Hydrodynamics Laboratory of the University of Strathclyde has been determined to be limited. Consequently, our focus in the subsequent discussions on multi-directional waves will be on the
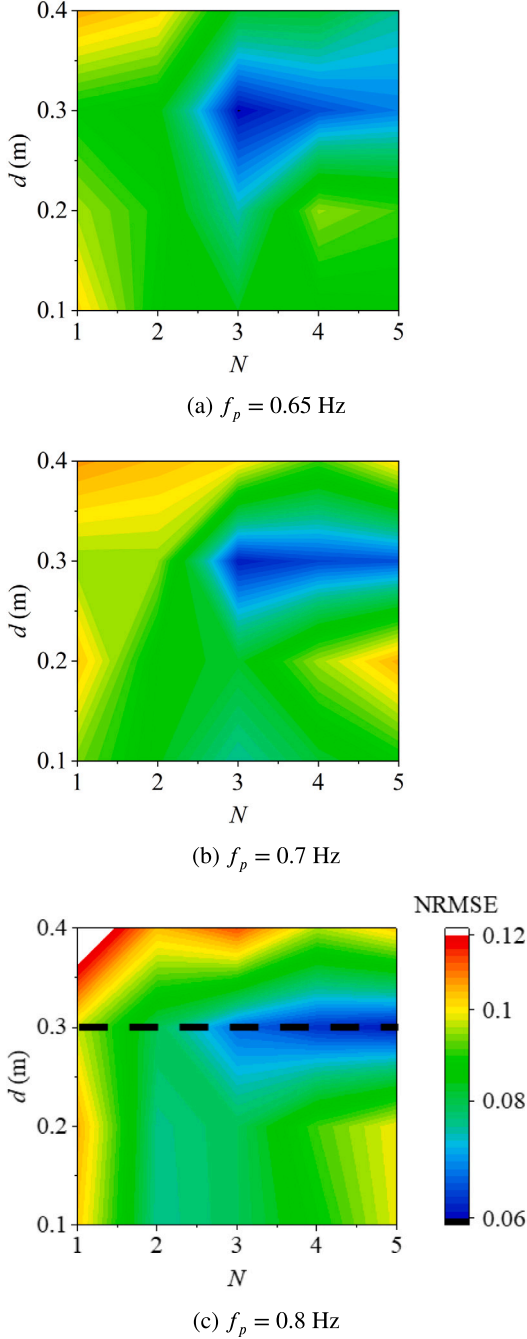
(a) $f_p = 0.65$ Hz

(b) $f_p = 0.7$ Hz

(c) $f_p = 0.8$ Hz

Fig. 18. Performance of the LSTM algorithm for the irregular wave cases.

Fig. 19. Predicted excitation force in the time domain of the irregular wave ($f_p = 0.8$ Hz, $T_f = 3$ s, $d = 0.3$ m).

integration of G with respect to the wave directional δ is 1 ensuring the wave energy (wave height) is equivalent to the corresponding unidirectional wave. The significant heights are different since G varies with δ.

$$G(\theta) = \frac{2^{2s-1}(\cos\frac{\theta}{2})^{2s}}{\pi(\Gamma(s)+1)^2\Gamma(2s+1)}. \tag{12}$$

where Γ is the gamma function of ordinals in statistics and

$$s = \begin{cases} s_p(\frac{\omega}{\omega_p})^5 & \omega < \omega_p \\ s_p(\frac{\omega}{\omega_p})^{-2.5} & \omega > \omega_p \end{cases} \tag{13}$$

$$s_p = 11.5(\frac{U\omega_p}{g})^{-2.5}. \tag{14}$$

The initial phase is random generated by a random function. 24 wave directions are calculated, and the wave spectrum is specified in each direction as

$$\eta(x,y,t) = \sum_{m=1}^{M_w}\sum_{n=1}^{N_\theta}\sqrt{2S(\bar\omega_m,\theta_n)d\omega d\theta}\hat\eta. \tag{15}$$

$$\hat\eta = \cos\left[\omega_{mn}t - k_{mn}(x\cos\theta_n + y\sin\theta_n) + \varepsilon_{mn}\right]. \tag{16}$$

where

$$\bar\omega_m = \frac{\omega_m - \omega_{m-1}}{2} \tag{17}$$

$$\omega_{mn} = \bar\omega_m - \frac{1}{2}d\omega + (n - 1 + \text{RAN}_{mn})\frac{d\omega}{N_\theta} \tag{18}$$

where RAN is a random number in the range of [0, 1]. Table 6 shows the values of critical characteristics of the directional spectrum. The power density is derived from statistics of a JONSWAP spectrum. The peak frequency is 6.5 Hz and the frequency varies from $0.1f_p$ (0.065 Hz) to $2.0f_p$ (1.3 Hz), since most of wave energy falls in this range. The increment of wave frequency is 0.05 Hz. There are total 26 frequency components being considered at each wave direction. The initial phases of wave components are generated randomly. The quantity of free parameters is $2 \times 26 \times 24$.

A total of eight wave probes are strategically positioned surrounding the position of floating structure, as depicted in Fig. 20. The distance

numerical simulation of wave prediction. It should be noted that the wave elevation and wave force discussed herein are based solely on simulation signals.

Multi-directional irregular wave scenarios incorporate the use of a directional spreading function, δ, to characterise the wave characteristics and generate time histories of multi-directional irregular wave elevations (Ji et al., 2015).

$$S(\omega,\theta) = S_0(\omega)G(\omega,\theta) \tag{11}$$

where S is the power density of directional spectrum, S_0 is the power density of frequency spectrum in one direction which is defined as P-M spectrum as used for the uni-directional irregular wave. G is defined as Mitsuyasu-type spreading function (Goda, 1999; Young, 1994). The
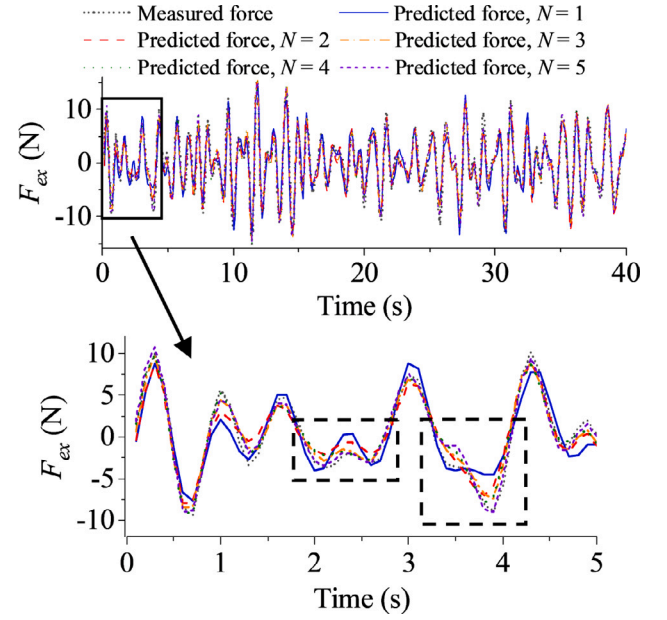
Table 6
Characteristics of the directional spectrum.

Spectrum characteristic	Value
H_s (m)	0.105
T_p (s)	1.54
γ	3.3
U_{10} (m/s)	0.4
Spreading component	24 (per 15 degrees)
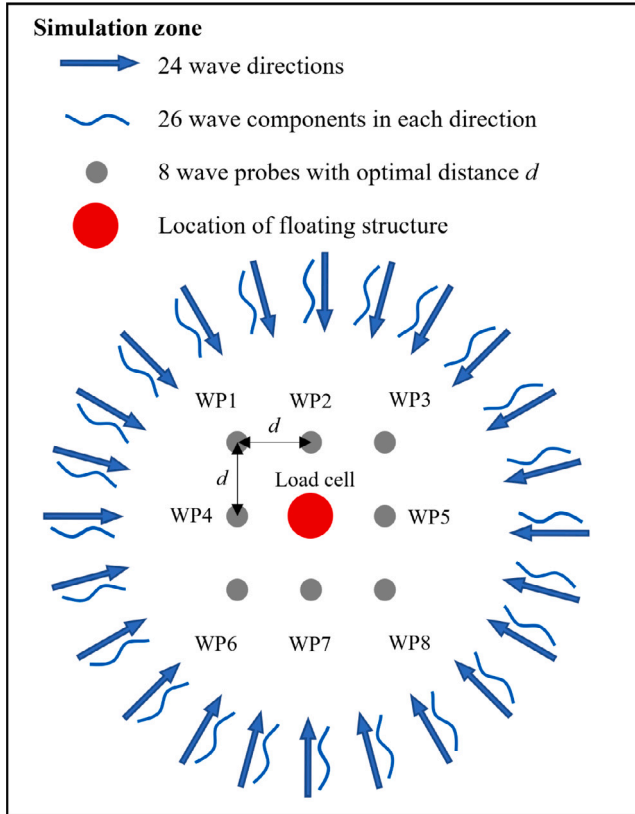
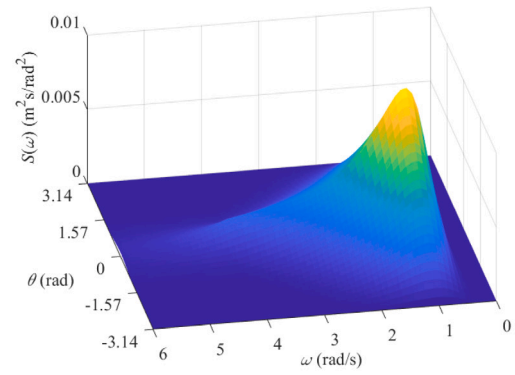Fig. 20. Measurement device distribution.

(a) Directional spectrum density distribution.

(b) Measurement values of wave heights and excitation force.
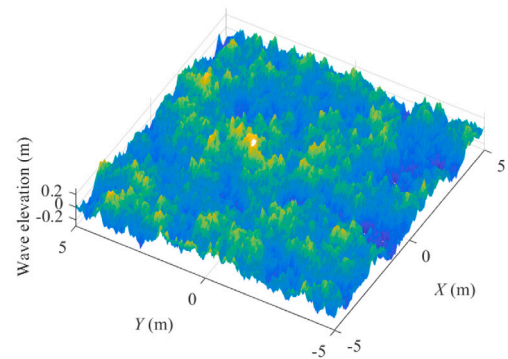
(c) A 5 m × 5 m wave surface based on the multi-directional wave spectrum density distribution.

Fig. 21. Simulation scenario of multi-directional irregular wave.

of neighbouring wave probes, d, is 0.3 m which is the optimal value for the wave prediction as discussed above. Fig. 21(a) shows the power density of the directional spectrum. Fig. 21(b) is the time history of wave elevation at the positions of eight wave probes, as well as wave force excited on the floating structure. Fig. 21(c) is the multi-directional wave pattern at the initial moment.

The time history of the wave elevations and excitation force covers a simulation of 2400 s under multi-directional irregular waves. The hyperparameters of the LSTM algorithm are shown in Table 7. It is assumed that the optimal parameters of the machine learning model, which are determined for the uni-directional wave cases, are also applicable to the multi-directional wave cases. Thus, the sampling frequency forward time can be determined.
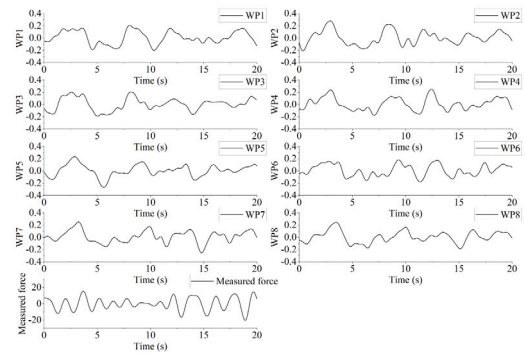
Fig. 22 presents the prediction results of the LSTM network for the multi-directional wave case. Similar to the results observed in the uni-directional cases, the predicted wave fails to accurately capture the peaks. However, the results still demonstrate the capability of the proposed LSTM-based wave prediction method when estimating multi-directional irregular waves.

*4.4. Comparison with Fourier-based wave prediction approach*

Fourier-based method is a classical technique, which is widely used to predict, analyse and describe the ocean waves in frequency

Table 7
Hyperparameters of the LSTM algorithm for the irregular wave cases.

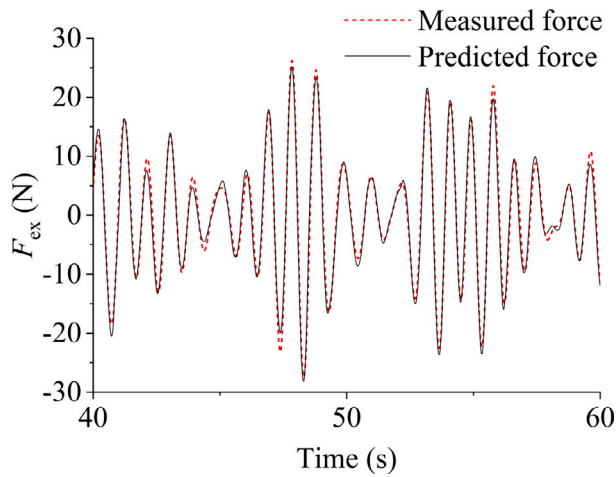| Parameter	Symbol	Unit	Value
Sampling frequency of dataset	f_s	Hz	20
Forward time	T_f	s	3
Total time	T_{total}	s	2400
Ratio of training data	R_{train}		0.9
Initial learning rate	$LR_{initial}$		0.01
Drop period of learning rate	N_{drop}		100
Number of LSTM hidden units	N_h		100
Iteration loops	N_{loop}		400

Fig. 22. Predicted excitation force in time domain of the multi-directional irregular wave.
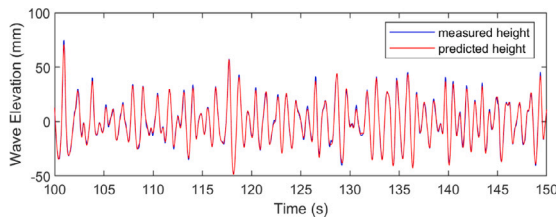

Fig. 23. Predicted wave elevation of Fourier-based method.

domain. It relies on the Fourier Transform (FT) and Invert Fourier Transform (IFT), which is a mathematical tool that decomposes a complex waveform into its constituent sinusoidal components with different frequencies, amplitudes, and phases (Falnes and Kurniawan, 2020). An extended maximum likelihood method is employed to determine the directional wave spreading, while the initial phases of directional free-wave components are determined using a least-square fitting scheme (Zhang et al., 1999). The Fourier-based method proposed in Halliday et al. (2011) and Duan et al. (2020) is adopted in the present study. The predicted wave elevation is satisfactory, as shown in Fig. 23.

The surge force transfer function, ψ_3, is obtained by using a potential flow method. The time-domain forces are obtained by using the transformation as shown in Eq. (19).

$$F_w(t) = \text{Re}\left[\sum_{j=1}^{N} \psi_3\left(\omega_j\right) A_j e^{i\left(\omega_j t + \epsilon_j\right)}\right] \tag{19}$$

The simulation result is adopted in the Fourier-based prediction, however, the LSTM-based consider the transfer function implicitly. LSTM can directly figure out the relationship between wave elevation and excitation forces from the measured data. Interpolation of surge force transfer function is illustrated in Fig. 24.

The predicted surge forces are shown in Fig. 25. While the phases of frequency components are accurately estimated, the amplitudes or peak values of the surge forces are not satisfactory. This discrepancy in amplitude is attributed to the linear assumption made in the potential flow calculation within the study. The calculation of the transfer function only accounts for the linear components of the wave force, whereas the measured force contains nonlinear components.

The perdition performance and computational cost of LSTM-based and Fourier-based methods are listed in Table 8. The prediction time horizon is determined as 24 s. The Fourier-based method has a fast computational speed. The Fourier-based method presents a higher computational speed, since it only needs to calculate the summation of the
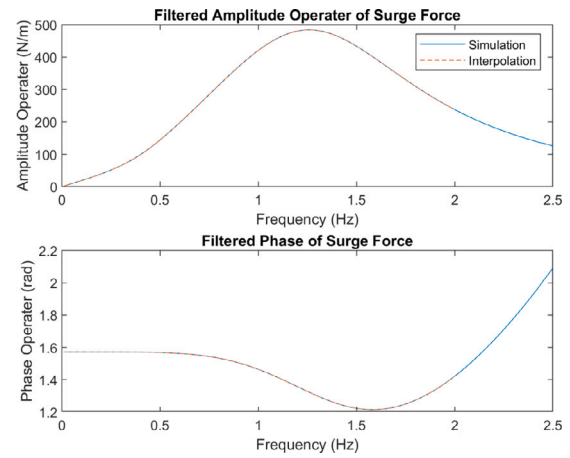

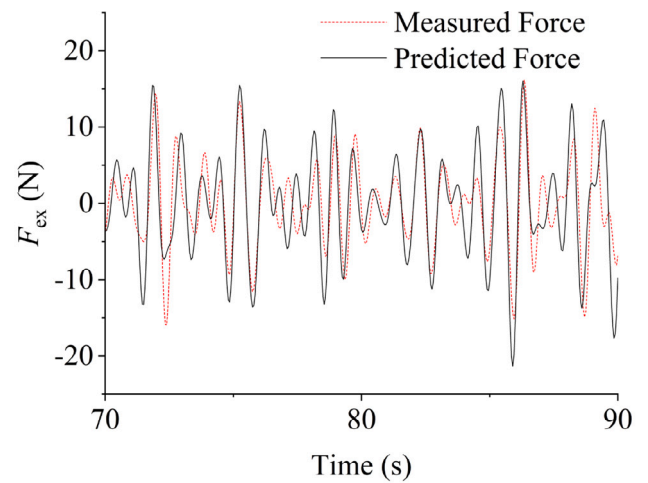**Fig. 24.** Predicted surge force based on Fourier method.

Fig. 25. Predicted surge force of Fourier-based method.

Table 8
Perdition performance and computational cost by LSTM-based and Fourier-based methods.

Prediction method	LSTM-based	Fourier-based
Actual predicted time (s)	24	24
Computational cost (s)	21.5	5.9
NMRSE of force prediction (–)	0.032	0.209

wave components. The LSTM-based method need to update the state cells of LSTM neural network at every step. It should be noted that the LSTM can deal with the nonlinear problems, which could potentially improve the prediction accuracy.

5. Conclusions

Prediction of wave excitation force is a key factor to influence power absorption efficiency in the real-time control of WEC. The present study introduces a LSTM RNN algorithm to identify the characteristics of wave excitation forces based on wave elevations. A total of 180 regular wave and 12 irregular wave tests are conducted initially. Compared with the results of experimental tests, the accuracy of the prediction results is verified, and the best parameters of the experimental setting are determined to guide the future tests. For the regular cases, one advantage of the proposed prediction method is that it can recognise high-order harmonic loads. In addition, the anti-noise capability of the

LSTM algorithm can filter random noises from the measured signals. This anti-noise characteristic is beneficial to small-scale model test. When the number of wave probes N increases from 1 to 2, the phase shift and peak fluctuation are eliminated. The proposed method is insensitive to N when $N > 2$. The increase in NRMSE in low frequency ranges is caused by the increase in SNR. The optimal setting of wave probes is $N = 4$ and $d = 0.3$ m for the regular cases. For the irregular cases in the study, the optimal sampling frequency is 20 Hz, and the optimal forward time is 3 s. The best NRMSE exists when $N = 4$ and $d = 0.3$ m for the irregular cases. $N = 3$ is also acceptable. The LSTM-based wave prediction method has potential to be used for multi-directional irregular waves. The predictive capacity of the LSTM-based wave prediction method has been demonstrated through numerical simulations. In order to further validate its performance, experimental tests will be conducted in a multi-directional wave tank to assess the accuracy and effectiveness of the prediction method. For further research, the results guide the experimental test of the real-time control using the same method. The performance of the method is validated in practical real-time control. The recognised high-order harmonic loads need to be quantified.

CRediT authorship contribution statement

Ming Zhang: Data curation, Formal analysis, Investigation, Methodology, Software, Validation, Writing – original draft, Writing – review & editing. **Zhi-Ming Yuan:** Conceptualization, Supervision, Writing – review & editing. **Sai-Shuai Dai:** Supervision. **Ming-Lu Chen:** Conceptualization, Funding acquisition, Supervision,Validation. **Atilla Incecik:** Supervision.

Declaration of competing interest

Data availability

No data was used for the research described in the article.

References

Babarit, A., Guglielmi, M., Clément, A.H., 2009. Declutching control of a wave energy converter. Ocean Eng. 36 (12–13), 1015–1024.

Cummins, W., 1962. The Impulse Response Function and Ship Motions. Report, David Taylor Model Basin Washington DC.

Deo, M.C., Sridhar Naidu, C., 1998. Real time wave forecasting using neural networks. Ocean Eng. 26 (3), 191–203. http://dx.doi.org/10.1016/S0029-8018(97)10025-7, URL: http://www.sciencedirect.com/science/article/pii/S0029801897100257.

Duan, Y., Lv, Y., Wang, F.-Y., 2016. Travel time prediction with LSTM neural network. In: 2016 IEEE 19th International Conference on Intelligent Transportation Systems. ITSC, IEEE, pp. 1053–1058.

Duan, W., Ma, X., Huang, L., Liu, Y., Duan, S., 2020. Phase-resolved wave prediction model for long-crest waves based on machine learning. Comput. Methods Appl. Mech. Engrg. 372, 113350.

Falnes, J., 1995. On non-causal impulse response functions related to propagating water waves. Appl. Ocean Res. 17 (6), 379–389.

Falnes, J., Kurniawan, A., 2020. Ocean waves and oscillating systems: linear interactions including wave-energy extraction, vol. 8, Cambridge University Press.

Fusco, F., Ringwood, J.V., 2012. A simple and effective real-time controller for wave energy converters. IEEE Trans. Sustain. Energy (ISSN: 1949-3029) 4 (1), 21–30.

Garcia-Abril, M., Paparella, F., Ringwood, J., 2017. Excitation force estimation and forecasting for wave energy applications. IFAC-PapersOnLine 50 (1), 14692–14697.

Goda, Y., 1999. A comparative review on the functional forms of directional wave spectrum. Coast. Eng. J. 41 (1), 1–20.

Greff, K., Srivastava, R.K., Koutník, J., Steunebrink, B.R., Schmidhuber, J., 2017. LSTM: A search space odyssey. IEEE Trans. Neural Netw. Learn. Syst. 28 (10), 2222–2232.

Halliday, J.R., Dorrell, D.G., Wood, A.R., 2011. An application of the fast Fourier transform to the short-term prediction of sea wave behaviour. Renew. Energy 36 (6), 1685–1692. http://dx.doi.org/10.1016/j.renene.2010.11.035.

Hillis, A., Brask, A., Whitlam, C., 2020. Real-time wave excitation force estimation for an experimental multi-DOF WEC. Ocean Eng. 213, 107788.

Hochreiter, S., Schmidhuber, J., 1997. Long short-term memory. Neural Comput. 9 (8), 1735–1780. http://dx.doi.org/10.1162/neco.1997.9.8.1735, URL: https://www.mitpressjournals.org/doi/abs/10.1162/neco.1997.9.8.1735.

Ji, X., Liu, S., Bingham, H.B., Li, J., 2015. Multi-directional random wave interaction with an array of cylinders. Ocean Eng. 110, 62–77.

Jin, S., 2019. Hydrodynamic and Control Optimization for a Heaving Point Absorber Wave Energy Converter (Ph.D. thesis). University of Hull.

Korde, U.A., Ringwood, J., 2016. Hydrodynamic Control of Wave Energy Devices. Cambridge University Press.

Li, G., Belmont, M.R., 2014. Model predictive control of sea wave energy converters– Part I: A convex approach for the case of a single device. Renew. Energy 69, 453–463.

Li, G., Weiss, G., Mueller, M., Townley, S., Belmont, M.R., 2012. Wave energy converter control by wave prediction and dynamic programming. Renew. Energy 48, 392–403.

Li, L., Yuan, Z., Gao, Y., 2018a. Maximization of energy absorption for a wave energy converter using the deep machine learning. Energy 165, 340–349. http://dx.doi.org/10.1016/j.energy.2018.09.093.

Li, L., Yuan, Z., Gao, Y., Zhang, X., 2018b. Wave force prediction effect on the energy absorption of a wave energy converter with real-time control. IEEE Trans. Sustain. Energy.

Ling, B.A., 2015. Real-Time Estimation and Prediction of Wave Excitation Forces for Wave Energy Control Applications (Ph.D. thesis). Oregon State University.

Mousavi, S.M., Ghasemi, M., Dehghan Manshadi, M., Mosavi, A., 2021. Deep learning for wave energy converter modeling using long short-term memory. Mathematics 9 (8), 871.

Neshat, M., Abbasnejad, E., Shi, Q., Alexander, B., Wagner, M., 2019. Adaptive neuro-surrogate-based optimisation method for wave energy converters placement optimisation. In: International Conference on Neural Information Processing. Springer, pp. 353–366.

Nguyen, H.-N., Tona, P., 2017. Wave excitation force estimation for wave energy converters of the point-absorber type. IEEE Trans. Control Syst. Technol. 26 (6), 2173–2181.

Ni, C., 2021. Data-driven models for short-term ocean wave power forecasting. IET Renew. Power Gener..

Rahoor, A., 2020. Comparison of Control Strategies for Wave Energy Converters (Ph.D. thesis). Uppsala University.

Salter, S.H., 1979. Power conversion systems for ducks. In: International Conference on Future Energy Concepts. pp. 100–108.

Son, D., Yeung, R.W., 2017. Optimizing ocean-wave energy extraction of a dual coaxial-cylinder WEC using nonlinear model predictive control. Appl. Energy 187, 746–757.

Valério, D., Mendes, M.J., Beirão, P., da Costa, J.S., 2008. Identification and control of the AWS using neural network models. Appl. Ocean Res. 30 (3), 178–188.

Young, I., 1994. On the measurement of directional wave spectra. Appl. Ocean Res. 16 (5), 283–294.

Zhang, W., 2014. Financial time series forecasting using neural networks.

Zhang, J., Yang, J., Wen, J., Prislin, I., Hong, K., 1999. Deterministic wave model for short-crested ocean waves: Part I. Theory and numerical scheme. Appl. Ocean Res. 21 (4), 167–188.

Zhang, M., Yuan, Z.-M., Dai, S.-S., Incecik, A., 2020. Development of a novel wave-force prediction model based on deep machine learning algorithms. In: The 30th International Ocean and Polar Engineering Conference. OnePetro.

Zhao, Q., Hu, X., Lin, J., Deng, X., Li, H., 2019. A novel short-term blood pressure prediction model based on LSTM. In: AIP Conference Proceedings. AIP Publishing, p. 020003.